Graphene-based rectangular nanotetramer patches for independent multiple Fano resonance modulation

WENJIE SHI[1], JICHENG WANG[1,2,*], LIFA HU[1,*]
[1]*School of Science, Jiangsu Provincial Research Center of Light Industrial Optoelectronic Engineering and Technology, Jiangnan University, Wuxi 214122, China*
[2]*State Key Laboratory of Applied Optics, Changchun Institute of Optics, Fine Mechanics and Physics, Chinese Academy of Sciences, Changchun 130033, China*

In this paper, we have proposed an uncomplicated novel graphene-based rectangular nanotetramer patches structure. The prominent single-band filter, graphene plasmon induced transparency, and dual plasmon induced transparency are obtained. Three optical modes can be achieved by the graphene nanoribbon response at different Fermi levels and lengths. These resonances can be adjusted at different frequencies by breaking the structure symmetry due to different formation mechanisms. The theoretical resonance peak fits well with the simulated data after performing a theoretical analysis of the physical mechanisms. The results help us to design optical devices based on plasmonic metasurfaces.

(Received March 24, 2022; accepted October 5, 2022)

Keywords: Graphene, Fano resonance, Plasmon-induced transparency, Parameter inversion method

1. Introduction

The quantum interference phenomenon occurs when the energy levels of the discrete and continuously excited state overlap in the atomic system. The narrow-band resonance spectrum of the discrete state and the broader spectrum of the continuous state interfere with each other through destructive or constructive interference to form an asymmetric Fano line [1]. Plasmon-induced transparency (PIT) is a novel phenomenon analogous to electromagnetically induced transparency and also is the particular case of Fano resonance [2]. The PIT generation is the consequence of the near-field coupling Fano interference, characterized by a significant transparent window in the spectrum because it eliminates the resonance absorption in system [3-5]. The Fano resonance provides great optical switching, modulation, and slow light opportunities with those advantages [6]. Several conventional methods can achieve the PIT response: bright mode-bright mode coupling, bright mode-dark mode coupling [7]. The bright mode [8] can directly generate a resonance effect under the excitation of an external electromagnetic field, and it has a strong coupling effect on the incident electromagnetic field [9, 10]. Furthermore, the dark mode usually cannot be directly excited by the incident electromagnetic field, but it can be indirectly excited by utilizing the neighboring bright mode structure to produce a resonance effect. The two coupling methods have different characteristics and unique application areas. The discovery of graphene has significantly expanded its application potential [11,12].

Graphene [13,14] is a typical two-dimensional crystal material with a single-layer thickness of only one atomic layer (about 0.35nm). Graphene may offer an efficient platform for application and research due to its superior optical and electrical performance [15,16]. The most significant advantage of graphene materials is that they can be adjusted by applying a bias electric field and an external magnetic field. Therefore, it is possible to manually control the PIT effect achieved by graphene-based materials and dynamically control the corresponding functional devices. In 2016, He X. et al. used the notch structure to successfully generate an induced transparent window under the coupling effect [17]. In 2017, Zhang Z. et al. induced a broadband transparent window based on the resonant frequency detuning caused by the asymmetry of the asymmetric rectangular graphene waveguide [18]. Xu H. et al. designed a continuous asymmetric graphene strip structure on a silicon substrate and successfully stimulated a double-band transparent window in 2018. Moreover, graphene has many applications in display devices [19, 20], plasma supersurfaces [21], laser devices [22, 23], optical fiber sensors [24, 25], super capacitors [26, 27], and photodetectors [28, 29]. In previous studies on the

formation of plasma-induced transparency, researchers mostly considered and analyzed simple structures [30, 31].

In this paper, we have designed an innovative tunable multifunctional graphene-based rectangular nanotetramer patches structure to achieve multiple-mode plasmonic-induced transparencies. The rectangular nanotetramer patches structure exhibits distinct singlet, double PIT, and double PIT responses in the transmission spectra by adjusting structural parameters. Based on the electric field diagrams at different frequencies, the PIT formation mechanism is analyzed. We have also regulated the geometrical parameters and Fermi levels of graphene nanoribbons to obtain an optimum combination for the PIT responses and utilized the parameter inversion to verify physical properties of the structure. The structure in this article possesses the advantage of dynamic adjustment so the PIT mode can be adjusted more flexibly.

2. Theoretical analysis

The results are analyzed using COMSOL Multiphysics through finite element methods to simulate the optical structure and thoroughly comprehend the Fano resonance by obtaining the transmission spectra. Fig. 1 illustrates the PIT schematic composed of four graphene nanoribbons attached to a substrate with a refractive index of 1.5. The geometric parameters of the four graphene patch arrays are as follows: A = 300 nm, P = 450 nm, w_1 = 30 nm, d = 10 nm, W = 50 nm, l = 120 nm, l_1 = 140 nm, l_2 = 170 nm, w_2 = 50 nm, D = 40 nm, respectively. The system is illuminated by the plane wave's incident angle in the Z direction, which is simply a TM polarized wave incident [32].

The surface conductivity of graphene σ, as well as the interband and intraband transitions, can all be expressed by Kubo formulas. According to the Kubo formula [33], graphene conductivity can be expressed as

$$\sigma_g(\omega, E_f, \tau, T) = \sigma_{intra} + \sigma_{inter} . \tag{1}$$

The physical parameters in this formula are described as follows: angular frequency ω, Fermi energy E_f, carrier relaxation τ, temperature T. Graphene conductivity is determined by adding σ_{intra} + σ_{inter}. σ_{intra} and σ_{inter} are contributed by intraband electron-photon scattering and direct interband electron transitions, respectively. The conductivity of graphene can be expressed in the form of the Kubo equation:

$$\sigma_{inter} = \frac{e^2}{4\hbar}\left[\frac{1}{2} + \frac{1}{\pi}\arctan\left(\frac{\hbar w - 2E_f}{2k_B T}\right)\right] - \frac{i}{2\pi}\ln\frac{\left(\hbar w + 2E_f\right)^2}{\left(\hbar w - 2E_f\right)^2 + 4\left(k_B T\right)^2} \tag{2}$$

$$\sigma_{intra} = \frac{2e^2 k_B T}{\pi\hbar^2}\frac{i}{\omega + i\tau^{-1}}\ln\left[2\cosh\left(\frac{E_f}{2k_B T}\right)\right]. \tag{3}$$

where $\tau = E_f\mu/ev_F^2$ is the relaxation time of carriers in graphene, $\hbar$ is the normalized Planck constant, e is the amount of electron charge, k_B is the Boltzmann constant, μ is the carrier mobility, $v_F \approx 10^6$ m/s is the Fermi speed, T = 300K is temperature.

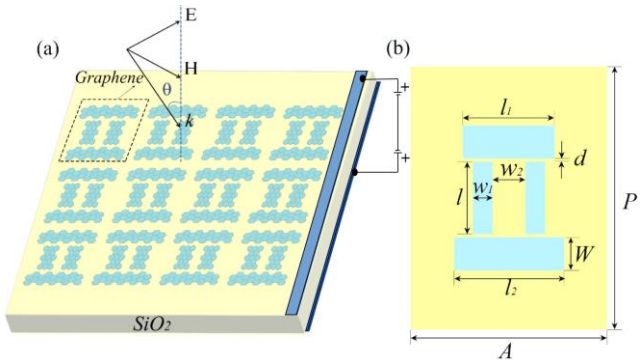

Fig. 1. (a) 3D schematic illustration of periodic graphene metamaterial device. (b) Top view of unit cell of the graphene metamaterial. The Fermi levels of structure can be adjusted simultaneously by imposing two independent bias voltages between the two gold gates and the SiO_2 substrate (color online)

For the terahertz band, the Kubo formula corresponding to the conductivity of graphene can be simplified as [34]

$$\sigma_g = \frac{ie^2 E_f}{\pi\hbar^2(\omega + i\tau^{-1})} \tag{4}$$

When the terahertz wave is incident, the graphene interband transition is in a forbidden state. Therefore, we set the graphene with a surface current density without thickness.

The dielectric constant, permeability, refractive index, and impedance can be retrieved from the reflection S_{11} and transmission S_{21} data. S_{11} represents the electromagnetic wave reflection parameter, S_{21} denotes the electromagnetic wave transmission parameter, and m is the material thickness. The relationship between the S parameter, refractive index n, and impedance z is given by

$$S_{11} = \frac{P_{01}(1 - e^{i2nk_0 m})}{1 - P_{01}^2 e^{i2nk_0 m}}, \tag{5}$$

$$S_{21} = \frac{\left(1 - P_{01}^2\right)e^{i n_0 k_r}}{1 - P_{01}^2 e^{i2 n_0 k_m}} \tag{6}$$

where $P_{01} = z - 1/z + 1$, and k_0 denotes the wave number of the incident wave in free space.

The refractive index n and impedance z are obtained by inversion of Eqs. (5) and (6) [35, 36], resulting in

$$z = \pm\sqrt{\frac{(1+S_{11})^2 - S_{21}^2}{(1-S_{11})^2 - S_{21}^2}}, \tag{7}$$

$$e^{ink_0m} = Q \pm i\sqrt{1-Q^2}, \tag{8}$$

where $Q = 1 - S_{11}^2 + S_{21}^2/2S_{21}$. Since the considered metamaterial is a passive medium, the symbol in the Eqs. (7) and (8) are determined by requirements

$$\mathrm{Rel}(z) \geq 0, \tag{9}$$

$$\mathrm{Im}(n) \geq 0, \tag{10}$$

where Rel(z) and Im(n) represent the real and imaginary part operators, respectively.

$$n = \frac{1}{k_0 d}\left\{\left[\left[\ln\left(e^{ink_0m}\right)\right]'' + 2b\pi\right] - i\left[\ln\left(e^{ink_0m}\right)\right]'\right\} \tag{11}$$

In Eq. (11), b is an integer related to the branch index of Rel(n). As mentioned above, the imaginary part of n is uniquely determined, but the branches of the logarithm function complicate the real part. The permeability and permittivity can be computed through the derivation above

$$\varepsilon = \frac{n}{z}, \tag{12}$$

$$\mu = n \cdot z \tag{13}$$

Based on the parameter inversion method, we can explore the PIT generation mechanism.

3. Numerical simulation results

The periodic boundary conditions were used in both x and y directions in this simulations. While broadband plane waves are incident from the z-direction, we apply a perfectly matched layer along the z-direction to absorb all light reaching the boundary. The accuracy of the results is ensured by using a non-uniform grid with the most significant element size smaller than 10% of the graphene surface plasmon's wavelength. The transmission spectra of only the upper graphene nanoribbon (UGN), lower graphene nanoribbon (LGN), left graphene nanoribbons (LRGN), and right graphene nanoribbons (GRNP) are measured to resolve the physical insights of PIT, as shown in Fig. 2. Meanwhile, we measured the electric field distribution at each point when E_f = 0.8 eV. Fig. 2(a) presents the incident light resonating with the UGN and the LGN. Then the transmittance in the spectrum decreases so that the UGN and LGN act as bright modes. The LRGN does not resonate with the incident light, as shown in Fig. 2(b) by the blue line. A hybrid map is drawn based on the electric field of the structure, as shown in Fig. 2(d). We use the electric field distribution diagram to explain the PIT formation mechanism more rigorously.

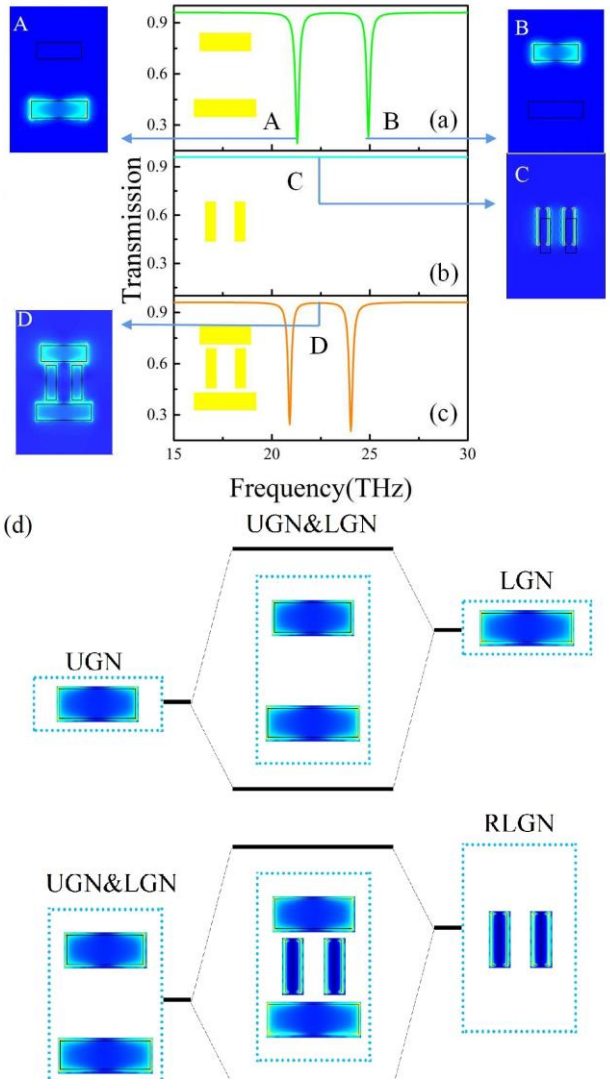

Fig. 2. (a)–(c) The transmission spectra of UGN, LGN, RLGN, and complete structure. The electric field distributions of the "A", "B", "C", "D", (d) Hybrid scheme of Graphene nanoribbons (color online)

The Fermi levels and geometric parameters of the bright modes can be regulated to achieve the single-band.

Fig. 3 displays how we can obtain the extinction ratio of the transmission spectra to achieve 94.1% in the range of 0.6 eV to 1.0 eV when $l_1 = l_2 = 140$ nm. As the Fermi level increases, the results demonstrate that the transmission peak frequency of the blue structure shifts from 21.4 THz to 27.6 THz, and the structure resonance grows. The number of charge carriers leads to the plasmonic oscillation surge with the increase of E_f, causing the transmission enhancement. The extinction ratio of the transmission can achieve 94.1%, indicating the structure has potential in the single-band filter.

Next, we continue to discuss the adjustable properties of the structure to explore PIT. As shown in Fig. 3, there is no PIT when the length of UGN and LGN are equal. Once $l_1 \neq l_2$, the PIT appears immediately. When the length of l_2 increases from 150 nm to 170 nm, the transmission peak gradually broadens, as shown in Fig. 4(a). It is evident that when l_2 = 170 nm, the PIT spectrum has excellent symmetry. We retain the optimized geometric parameters, and the PIT at different frequencies can be achieved by adjusting the Fermi level of graphene, as shown in Fig. 4(b). Afterward, we enhance the dynamically tunable properties of graphene by adjusting the Fermi level of the green part to achieve the PIT more extensively, as shown in Fig. 4(c).

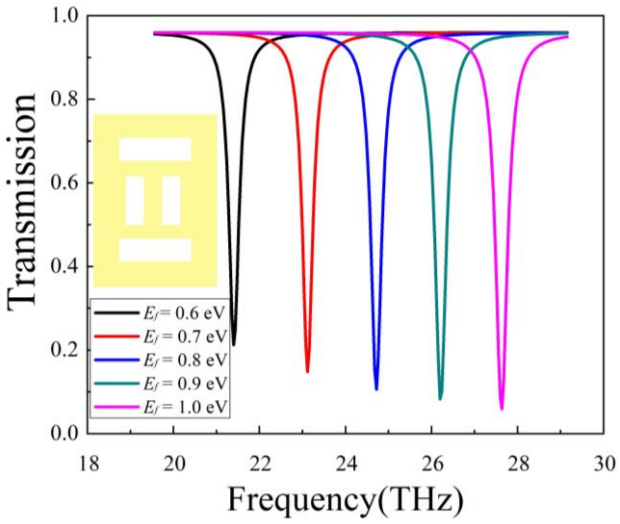

Fig. 3. The transmission spectra of different Fermi levels, when $l_1 = l_2 = 140$ nm (color online)

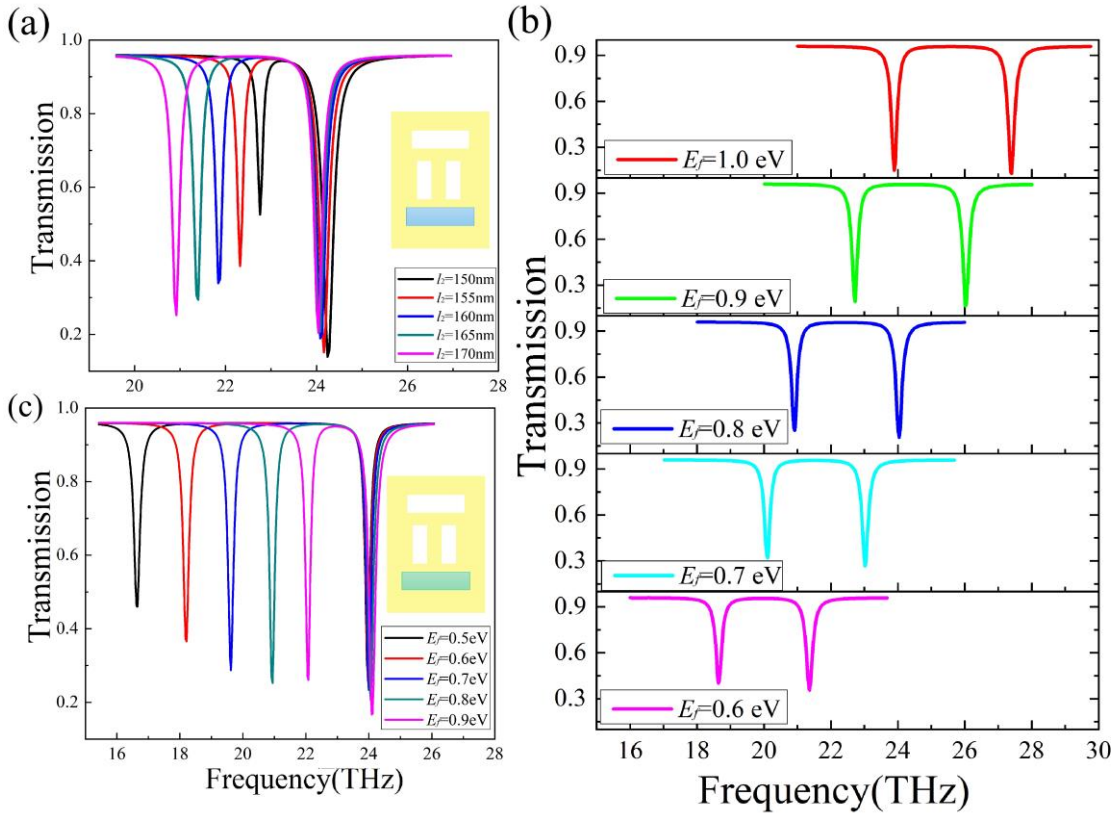

Fig. 4. (a) The transmission spectra of changing the length of the blue part of the graphene nanoribbons. (b) The transmission spectra of different Fermi levels, when $l_1 = 140$ nm, $l_2 = 170$ nm. (c) The transmission spectra of changing the Fermi level of the green part of the graphene nanoribbon, when $l_1 = 140$ nm, $l_2 = 170$ nm (color online)

It is universally known that metal or dielectric metamaterial structures are hard to remold after manufacturing. We exploit the potential of graphene to break the structural symmetry by changing the nanoribbon Fermi level without changing the geometrical parameters of the structure, as shown in Fig. 5(a). It depicts the transmission spectrum of the system as a function of the Fermi level of the orange part and frequency. The double PIT can be achieved by adjusting the $E_{f2.}$ When E_{f2} = 0.5 eV, double PIT appears, with the increase of the Fermi level on the left, the effect of the III peaks is gradually apparent. Besides, the structure can realize the conversion of TM and TE polarized waves. The corresponding frequencies of the three peaks are 20.73 THz, 22.94 THz, and 24.89 THz when E_{f2} = 0.6 eV, as shown in Fig. 5(b). The TM wave then changes to the TE polarized wave, and the peaks become 22.94 THz, 24.89 THz, and 22.27 THz. We can use the structure to achieve a TE/TM mode switch with some performances based on this phenomenon. In theory, if we continue to break the symmetry of the structure, the triple PIT also can be appeared, but it is not repeated in this article.

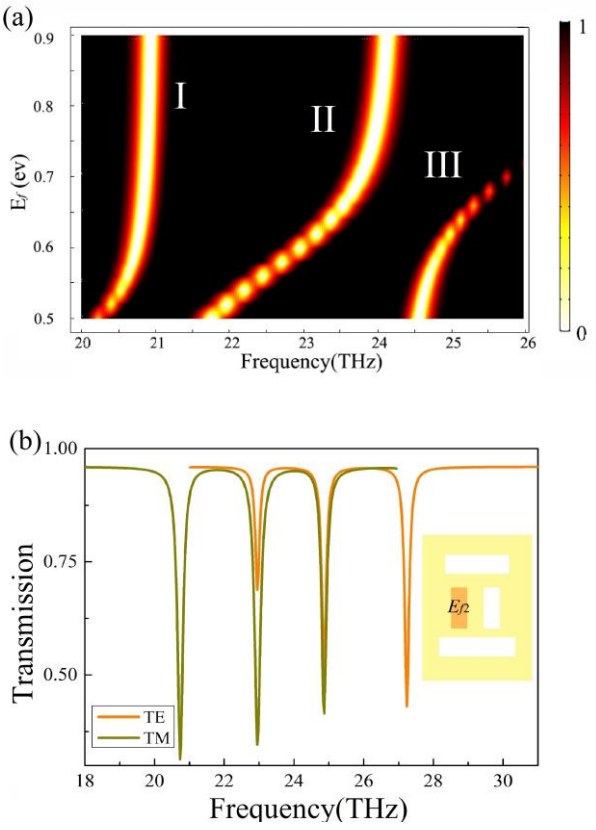

Fig. 5. (a) Transmission spectra as a function of the frequency and the red part's Fermi energy level, when l_1 = 140 nm, l_2 = 170 nm. (b) The transmission spectra of TE and TM, When E_{f2} = 0.6eV (color online)

Based on the updated parameter inversion method, we found the permeability and dielectric constant, refractive index, and impedance of the system when E_f = 0.8 eV, E_{f2} = 0.6 eV, as shown in Fig. 6. When the dielectric constant and permeability are negative, the incident electromagnetic wave passes through the filter with a slight attenuation, and the electromagnetic wave loss is the lowest for electromagnetic metamaterial filters. When the dielectric constant and magnetic permeability have different signs, most of the incident electromagnetic waves are reflected on the metasurface filter surface and cannot pass, as shown in Fig. 6 (a). We found that the changing trend of refractive index and impedance is almost the same, and the red line, green line, and blue line correspond well to the stop-band resonance point, as shown in Fig. 6(b). The reason for these phenomena is that electromagnetic waves and light have similar refraction characteristics. When electromagnetic waves pass these frequency points, the refractive index of the metamaterial filter suddenly changes, affecting the propagation path of typical incident electromagnetic waves. Subsequently, the electromagnetic waves cannot surpass the metamaterial medium, promoting the generation of stop-band resonance points, as shown in Fig. 5(b).

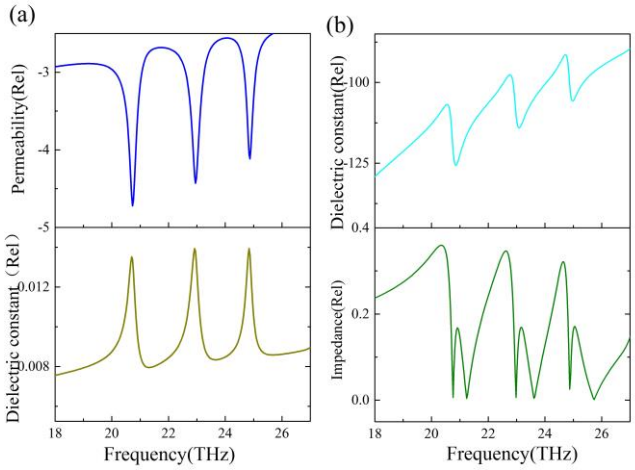

Fig. 6. (a)The permeability and dielectric constant of double PIT (b) The refractive index and impedance of double PIT (color online)

4. Conclusion

In this paper, we have studied graphene-based rectangular nanotetramer patches for independent multiple Fano resonance modulation. We exploit a parameter inversion to obtain the generation mechanism of PIT. In simulation and theory, the geometric parameters and Fermi levels were changed to obtain singlet, double PIT, and double PIT responses. When maintaining the UGN and

LGN symmetry of the structure, we can achieve a frequency tunable filter by adjusting the Fermi levels, and the extinction ratio can achieve 94.1%. The PIT can be realized by breaking the structure symmetry, and it can be achieved at 16 THz to 28 THz by taking advantage of dynamically tunable graphene. We exploit the potential of graphene to break the symmetry of the LRGN to obtain double PIT. Besides, the structure can realize the conversion of TM and TE polarized waves. The system can be used in terahertz band-stop filter and tunable frequency range and double PIT window metamaterial with transparency windows.

Acknowledgments

This work was supported in part by the National Natural Science Foundation of China (11811530052), the Intergovernmental Science and Technology Regular Meeting Exchange Project of Ministry of Science and Technology of China (CB02-20), the Open Fund of State Key Laboratory of Applied Optics (SKLAO2020001A04), and the Training Programs of Innovation and Entrepreneurship for Undergraduates of Jiangsu Province and China (201910295067).

References

[1] U. Fano, Phys. Rev. **124**, 1866 (1961).
[2] Z. Li, Y. Ma, R. Huang, R. Singh, J. Gu, Z. Tian, J. Han, W. Zhang, Opt. Express **19**, 8912 (2011).
[3] A. N. Grigorenko, M. Polini, K. S. Novoselov, Nat. Photonics **6**, 749 (2012).
[4] J. Valentine, S. Zhang, T. Zentgraf, E. Ulin-Avila, D. A. Genov, G. Bartal, X. Zhang, Nature **455**, 376 (2008).
[5] M. Gerken, D. A. Miller, Appl. Optics **42**, 1330 (2003).
[6] S. Zhan, H. Li, Z. He, B. Li, Z. Chen, H. Xu, Opt. Express **23**, 20313 (2015).
[7] Z. Zhang, X. Zang, Y. Long, P. Ma, L. Liao, H. Li, J. Lightwave Technol. **35**, 5020 (2017).
[8] B. Tang, L. Dai, C. Jiang, Opt. Express **19**, 628 (2011).
[9] X. Yang, X. Hu, Z. Chai, C. Lu, H. Yang, Q. Gong, Appl. Phys. Lett. **104**, 221114 (2014).
[10] N. Liu, L. Langguth, T. Weiss, J. Kästel, M. Fleischhauer, T. Pfau, H. Giessen, Nat. Mater. **8**, 758 (2009).
[11] Y. Qin, F. Zhou, Z. Liu, X. Zhang, S. Zhuo, X. Luo, C. Ji, G. Yang, Z. Zhou, L. Sun, T. Liu, J. Opt. Soc. Am. A-Opt. Image Sci. Vis. **39**, 377 (2022).
[12] C. Wu, A. B. Khanikaev, G. Shvets, Phys. Rev. L. **106**, 107403 (2011).
[13] K. S. Novoselov, A. K. Geim, S. V. Morozov, D. Jiang, Y. Zhang, S. V. Dubonos, I. V. Grigorieva, A. A. Firsov, Science **306**, 666 (2004).
[14] Y. Fan, N. Shen, F. Zhang, Q. Zhao, H. Wu, Q. Fu, Z. Wei, H. Li, C. M. Soukoulis, Adv. Opt. Materials **7**(3), 1800537 (2019).
[15] N. M. R. Peres, Rev. Mod. Phys. **82**, 2673 (2010).
[16] S. Xiao, T. Wang, T. Liu, C. Zhou, X. Jiang, Journal of Phys. D: Applied Phys. **53**(50), 503002 (2020).
[17] X. He, Q. Zhang, G. Lu, G. Ying, F. Wu, J. Jiang, RSC Adv. **6**, 52212 (2016).
[18] H. Xu, M. Zhao, C. Xiong, B. Zhang, M. Zheng, J. Zeng, H. Xia, H. Li, Phys. Chem. **20**, 25959 (2018).
[19] U. Kim, J. Kang, C. Lee, H. Y. Kwon, S. Hwang, H. Moon, J. C. Koo, J. Nam, B. H. Hong, J. Choi, H. R. Choi, Nanotechnology **24**, 145501 (2013).
[20] H. Park, P. R. Brown, V. Bulovic, J. Kong, Nano Lett. **12**, 133 (2012).
[21] P. Avouris, M. Freitag, IEEE J. Sel. Top. Quantum Electron. **20**, 72 (2013).
[22] A. N. Grigorenko, M. Polini, K. S. Novoselov, Nat. Photonics **6**, 749 (2012).
[23] C. Zhang, C. Long, S. Yin, R. G. Song, B. H. Zhang, J. W. Zhang, D. P. He, Q. Cheng, Applied Optics **206**, 109768 (2021).
[24] Z. Sun, T. Hasan, F. Torrisi, D. Popa, G. Privitera, F. Wang, F. Bonaccorso, D. M. Basko, A. C. Ferrari, ACS Nano **4**, 803 (2010).
[25] C. Zhang, C. Long, S. Yin, R. G. Song, B. H. Zhang, J. W. Zhang, D. P. He, Q. Cheng, Mater. Des. **06**, 109768 (2021).
[26] C. Liu, Z. Yu, D. Neff, A. Zhamu, B. Z. Jang, Nano Lett. **10**, 4863 (2010).
[27] B. Xiao, S. Tong, A. Fyffe, Z. Shi, Opt. Express **28**(3), 4048 (2020).
[28] S. Gong, B. Xiao, L. Xiao, S Tong, S. Xiao, Opt. Mater. Express **9**(1), 35 (2019).
[29] W. Cai, B. Xiao, J. Yu, L. Xiao, Opt. Communications **475**, 126266 (2020).
[30] Z. Sun, H. Chang, ACS NANO **8**, 4133 (2014).
[31] F. H. Koppens, T. Mueller, P. Avouris, A. C. Ferrari, M. S. Vitiello, M. Polini, Nat. Nanotechnol. **9**, 780 (2014).
[32] Y. Niu, J. Wang, Z. Hu, F. Zhang, Opt. Commun. **416**, 77 (2018).
[33] J. Liu, Y. Zhou, L. Li, P. Wang, A. V. Zayats, Opt. Express **23**, 12524 (2015).
[34] B. Xiao, J. Zhu, L. Xiao, Applied Optics **59**(20), 6041 (2020).
[35] P. Markos, C. Soukoulis, Opt. Express **11**, 649 (2003).
[36] D. R. Smith, S. Schultz, P. Markoš, C. M. Soukoulis, Phy. Rev. B **65**, 195104 (2002).

*Corresponding author: jcwang@jiangnan.edu.cn